Comparison of reduction products from graphite oxide and graphene oxide for anode applications in lithium-ion batteries and sodium-ion batteries†

Yige Sun,[a,b] Jie Tang,*[a,b] Kun Zhang,[a] Jinshi Yuan,[a] Jing Li,[a,b] Da-Ming Zhu,[c] Kiyoshi Ozawa[a] and Lu-Chang Qin[d]

Hydrazine-reduced graphite oxide and graphene oxide were synthesized to compare their performances as anode materials in lithium-ion batteries and sodium-ion batteries. Reduced graphite oxide inherits the layer structure of graphite, with an average spacing between neighboring layers (*d*-spacing) of 0.374 nm; this exceeds the *d*-spacing of graphite (0.335 nm). The larger *d*-spacing provides wider channels for transporting lithium ions and sodium ions in the material. We showed that reduced graphite oxide as an anode in lithium-ion batteries can reach a specific capacity of 917 mA h g^{-1}, which is about three times of 372 mA h g^{-1}, the value expected for the LiC_6 structures on the electrode. This increase is consistent with the wider *d*-spacing, which enhances lithium intercalation and de-intercalation on the electrodes. The electrochemical performance of the lithium-ion batteries and sodium-ion batteries with reduced graphite oxide anodes show a noticeable improvement compared to those with reduced graphene oxide anodes. This improvement indicates that reduced graphite oxide, with larger interlayer spacing, has fewer defects and is thus more stable. In summary, we found that reduced graphite oxide may be a more favorable form of graphene for the fabrication of electrodes for lithium-ion and sodium-ion batteries and other energy storage devices.

1. Introduction

Despite recent progress and success in exploring new electrode materials, such as Si, for lithium-ion batteries (LIBs),[1,2] carbon-based electrodes, such as graphene,[3] CNTs,[4] hard carbon,[5] soft carbon,[6] and graphite,[7] remain the dominant materials for LIBs and other energy storage devices. Among the carbon-based electrode materials, graphite is the most widely used electrode material for LIBs due to its excellent electrical conductivity, layered crystals, and low-cost for mass production.[7] Since their successful isolation in 2004, graphene-single atomic layered sheets have been considered to be a more promising electrode material for various energy storage devices.[8,9] Intensive studies regarding novel procedures for synthesizing graphene sheets and the properties of graphene as an electrode material have been conducted in the past decade due to the unusual mechanical and electronic properties, such as high surface area, large surface-to-volume ratio, high electrical conductivity, and high chemical and thermal tolerance, of graphene.[3,8–10]

Many of these carbon products can be produced from the same parent materials; the same product can be made through several different chemical or physical pathways or channels. For example, graphene can be synthesized from graphite through two different routes: one is to create graphite oxide first through Hummer's method,[11,12] followed by a reduction reaction to produce graphene; the other is to produce graphene oxide from graphite oxide first through mechanical methods, such as ultrasonication or centrifugation,[13] followed by chemical reduction of the graphene oxide to graphene.[14] Fig. 1(a) illustrates these two different routes for synthesizing graphene from graphite.

Ruoff's group systematically studied the mechanisms of graphite oxide and graphene oxide formation in 2010.[13] They reported that suitable ultrasonic treatment can exfoliate graphite oxide into very thin graphene oxide sheets.[11,13,14] The individual layers present in graphene oxide are not as topologically constrained as the layers in graphite oxide. A few years later,

[a]*National Institute for Materials Science, 1-2-1 Sengen, Tsukuba 305-0047, Japan. E-mail: tang.jie@nims.go.jp*
[b]*Doctoral Program in Materials Science and Engineering, University of Tsukuba, 1-1-1 Tennodai, Tsukuba 305-8577, Japan. E-mail: tang.jie@nims.go.jp*
[c]*Department of Physics and Astronomy, University of Missouri-Kansas City, Kansas City, Missouri 64110, USA*
[d]*Department of Physics and Astronomy, University of North Carolina at Chapel Hill, Chapel Hill, NC 27599-3255, USA*
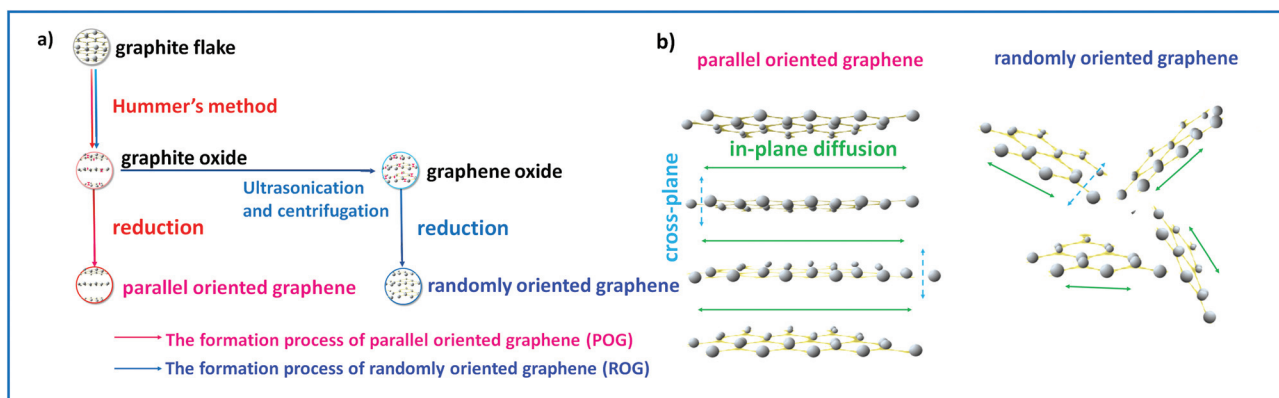†Electronic supplementary information (ESI) available. See DOI: 10.1039/c6nr07650e

Fig. 1 (a) The formation process of graphite oxide, graphene oxide, parallel oriented graphene (POG) and randomly oriented graphene (ROG). (b) Schematic of in-plane lithium diffusion and cross-plane diffusion for parallel and randomly oriented graphene.

reduced products from both graphite oxide and graphene oxide were studied.[14] The reduction product of graphene oxide exhibited a randomly oriented structure.[11,14] Meanwhile, reduced graphite oxide showed slight delamination during reduction, which was not exfoliated along with the outer layers.[14] The chemical reduction degree and surface area of reduced graphite oxide were lower than those of reduced graphene oxide, indicating that these two reduction products have different chemical and structural properties.[11,14]

Although graphene can be produced through different reaction pathways or routes, the final products have drastically different morphologies, uniformities, defect concentrations, *etc*. We found and will present in this paper below that graphene produced through the reduction of graphite oxide has a tendency to align individual graphene sheets in the same direction within each domain in a signature inherited from the "parent" graphite. However, the morphology of graphene produced from reduction of graphene oxide suggests that the individual graphene sheets are randomly oriented without any alignment. Fig. 1(b) illustrates the differences in the morphologies of graphene sheets produced through these two similar yet different routes. For the purpose of distinguishing the morphologies of graphene produced *via* the two different routes described above and for the convenience of presenting the results clearly, we refer to graphene produced *via* reduction of graphite oxide as "parallel oriented graphene (POG)" and graphene created *via* reduction of graphene oxide as "randomly oriented graphene (ROG)". The morphology differences between POG and ROG are sensitive to the preparation conditions. There are chemical and structural differences between graphite oxide and graphene oxide.[14] The differences between graphite oxide and graphene oxide lead to the morphology differences between POG and ROG.

In this work, we synthesized graphene using the two methods described above. We systematically compared their microscopic structures and morphologies. We thoroughly examined their electrochemical performances as anode materials in lithium-ion batteries. We found that graphene produced directly from the reduction of graphite oxide shows better performance as an anode material in LIBs. The specific capacity reached 917 mA h g^{-1} at a current density of 50 mA g^{-1}. The differences between their electrochemical performances during sodium ion intercalation and de-intercalation are even more obvious because the ionic radius of Na$^+$ (0.95 Å) is larger than that of Li$^+$ (0.65 Å).[15] The differences in the performance of graphene produced through the two different routes can be understood in terms of their morphologies and microscopic structures.

2.   Experimental

2.1   Synthesis of graphite oxide and parallel oriented graphene (POG)

In our study, graphite oxide was prepared using a modified Hummer's method which was described in detail in an earlier report.[11,14] In this process, graphite flakes and NaNO$_3$ were mixed. Then, H$_2$SO$_4$ was added to the mixture in an ice water bath, followed by addition of KMnO$_4$. After further stirring for 12 hours, deionized water was added to the suspension. Finally, H$_2$O$_2$ was added to the mixture to reduce excess KMnO$_4$. The mixture formed a yellow graphite oxide suspension. Although the detailed structure of graphite oxide is unclear, the most probable structural models reported are the Dékány model[16] and the Lerf–Klinowski model,[17] in which the graphite oxide retains a "stacked structure similar to graphite" but has myriad oxide functionalities with larger spacing than graphite.[13,18]

In this work, hydrazine reduction as a soft method was used instead of conventional physical methods, such as thermal reduction,[19] to maintain the "stacked structure" of graphite oxide. In this method, the graphite oxide suspension was diluted to 0.5 mg mL^{-1} directly using deionized water without exfoliation. Then, hydrazine monohydrate (3 μL for 3 mg graphite oxide) was added to the solution while it was continuously stirred at 98 °C for 24 hours. After the stirring

process, the mixture was filtered and washed with distilled water at least 5 times until the pH reached 7, and the parallel oriented graphene was acquired in the form of a black powder.

2.2 Synthesis of randomly oriented graphite (ROG) using graphene oxide exfoliated from graphite oxide

In this route, exfoliated graphite oxide was produced from graphite *via* the same procedure described in the section above. There are many methods to exfoliate graphite oxide into graphene oxide, such as sonication and stirring.[12] In our study, the sonication method was used to create graphene oxide. It was reported that this method tends to introduce defects or even cause damage to the graphene platelets.[12,13] We sonicated graphite oxide in deionized water for 30 min and then centrifuged it at 35 000 rpm to obtain the graphene oxide precipitation. This process was repeated 5 times to ensure the full exfoliation of graphite oxide to graphene oxide.

When synthesizing graphene from graphene oxide, hydrazine monohydrate (3 μL for 3 mg graphene oxide) was added to the graphene oxide suspension (0.5 mg mL^{-1}), followed by reflux at 98 °C for 24 hours. The graphene, in the form of a black powder, was filtered and washed by the same process described in section 2.1.

2.3 Fabrication of graphene electrodes

In order to compare the performance of electrodes fabricated from graphene obtained *via* two different routes, we fabricated two electrodes, each made from a graphene material acquired through either the red or blue route described above. To fabricate the electrodes, graphene powder was dispersed in ethanol to form a suspension. The suspension was then filtered through a weighted porous filter membrane (47 mm Hydrophilic PTFE membrane filter with a 0.2 μm pore size, Merck Millipore). To remove water and ethanol, the membrane was dried in vacuum for 24 hours. After that, the dried membranes were cut into circular disks (15 mm diameter) and then dried at 110 °C in vacuum for 12 hours. The disks with activated material were used as the electrodes in coin cells.

2.4 Structural characterization

The morphologies of graphene produced *via* the procedure described in 2.1 and 2.2 were examined using a scanning electron microscope (SEM) and a high resolution transmission electron microscope (HRTEM) to examine their microscopic structures. The microscopic structures and the chemical compositions of the graphene samples were characterized through X-ray powder diffraction, X-ray photoelectron spectroscopy, and Raman spectroscopy. To characterize the structural changes due to lithium ion intercalation, an airtight sample chamber was used to isolate the samples from air.

2.5 Adsorption isotherm characterization

Nitrogen gaseous adsorption–desorption isotherm measurements were performed on the two graphene samples at −196 °C in an Autosorb-1 (Quantachrome Instruments). Before N$_2$ adsorption, both samples were outgassed at 150 °C under vacuum for 24 hours. The Brunauer–Emmett–Teller (BET) equation was used to calculate the specific surface areas. The density functional theory (DFT) model (supplied by Quantachrome Autosorb ASiQwin 2.0) was used to calculate the pore size distributions.

2.6 Electrochemical performance

The electrochemical properties of the electrodes fabricated from the two types of graphene were individually characterized through impedance measurements using a four-probe method. The rate and cycling performances of these electrodes were tested by assembling them in CR2032-type coin cells in an argon environment. The cells were constructed with the graphene as the active working electrode, a piece of lithium foil as the reference and counter electrode, and a piece of copper foil as the current collector. A piece of polypropylene was used as the separator in the cell, and LiPF$_6$ (1 mol L^{-1} in EC : DMC = 1 : 1 (v/v %)) was used as the electrolyte in the cell. Sodium foil and NaPF$_6$ electrolyte (1 mol L^{-1} in EC : DMC = 1 : 1 (v/v %)) were used to replace lithium foil and LiPF$_6$ electrolyte to assemble sodium-ion batteries (SIB). The cells were galvanostatically charged and discharged under different current densities; also, cyclic voltammetry measurements were carried out at room temperature.

2.7 Characterization of graphene electrode lithium intercalation

We further characterized the structural changes occurring in the two different graphene samples after lithium intercalation. Fig. 6 shows the X-ray diffraction pattern of the graphene electrode after lithium intercalation. The inset shows the airtight sample chamber that was used to protect the sample from exposure to air after the intercalation. In order to achieve lithium ion intercalation in this measurement, the coin cells were first discharged and charged for 3 cycles, then discharged to 0.01 V to insure full lithium ion intercalation into the anode.

2.8 Li$^+$/Na$^+$ diffusion coefficient and exchange current density calculation

Electrochemical impedance spectroscopy (EIS) measurements for both types of graphene were performed at a 50% state of charge (SOC) in the AC frequency (from 200 kHz to 0.01 Hz) using a Biologic VMP-3 model potentiostat. The lithium ion and sodium ion diffusion coefficients, as well as the exchange current density, can be calculated according to eqn (1) and (2):[20–23]

$$j_0 = \frac{RT}{nFR_{ct}A} \qquad (1)$$

$$D = \frac{R^2 T^2}{2A^2 n^4 F^4 C^2 \sigma^2} \qquad (2)$$

where j_0 is the exchange current density, indicating the reversibility of the electrochemical reaction, D is the diffusion coefficient of lithium ions or sodium ions, R is the gas constant

Table 1 Kinetic parameters of POG and ROG electrodes in lithium-ion batteries and sodium-ion batteries

Sample	R_{b} (Ω)	R_{ct} (Ω)	D (10^{-11} cm^2 s^{-1})	j_0 (10^{-4} A cm^{-2})
POG (Li$^+$)	6.99	67.92	2.12	9.28
ROG (Li$^+$)	7.87	312.08	0.55	1.48
POG (Na$^+$)	64.62	222.40	0.53	1.77
ROG (Na$^+$)	72.39	428.93	0.083	0.68

(8.314 J K^{-1} mol^{-1}), T is the absolute temperature (298.15 in this work), n is the number of transferred electrons, F is the Faraday constant (96 500 C mol^{-1}), R_{ct} is deduced from modeling as shown in Table 1, A is the surface area of the electrode (A = specific surface area × mass of active electrode), C is the concentration of Li$^+$ or Na$^+$, and σ is the Warburg factor (the slope of line $Z' \sim \omega^{-1/2}$, as shown in Fig. 11(b) and 12(d), because $Z' = R_{ct} + \sigma\omega^{-1/2}$).

3. Experimental

3.1 Structural characterization and morphology

Fig. 2 and S1† depict the SEM and HRTEM micrographs obtained on the two types of graphene samples produced *via* direct reduction of graphite oxide and *via* transformation of graphite oxide into graphene oxide followed by reduction of graphene oxide. These micrographic images show distinct differences in the microscopic morphologies of the graphene sheet assemblies obtained through the two different routes: graphene assembly produced from the direct reduction of

graphite oxide shows a domain structure with an average domain size of about 10 nm. Within each domain, the graphene sheets are oriented approximately in parallel, as shown in Fig. 2(a) and (c). The intensity profiles along lines perpendicular to the parallel sheets enable an approximate determination of the average distance between the neighbouring graphene sheets. Fig. 2(e) and (f) show the intensity profiles along the lines indicated in Fig. 2(c) and (d), respectively. For graphene obtained from reduction of graphite oxide, the average distance between neighbouring graphene sheets is 0.37 nm. For graphene obtained from reduction of graphene oxide, the intensity line profile does not display any periodic structure, as shown in Fig. 2(f); this indicates that the graphene sheets are probably randomly orientated. The difference between the microscopic morphologies of the two types of graphene indicate that POG may inherit the layered structure of graphite, while the layered structure is completely destroyed in ROG. The selected area electron diffraction (SAED) patterns of POG and ROG (inset images in Fig. 2(c) and (d)) show three rings ((110), (221) and (002) lattice planes), which indicates that both electrodes are amorphous.

3.2 Chemical characterization and adsorption isotherms

It is important to rule out the possibility that this morphological difference reflects the slightly different chemical compositions of the two types of graphene. Fig. 3 and 4 show the X-ray photoelectron and Raman spectra of the POG and ROG samples, respectively.

As shown in Fig. 3, the C$_{1s}$ spectrum of the samples can be deconvoluted into several sub-peaks (graphitic carbon with
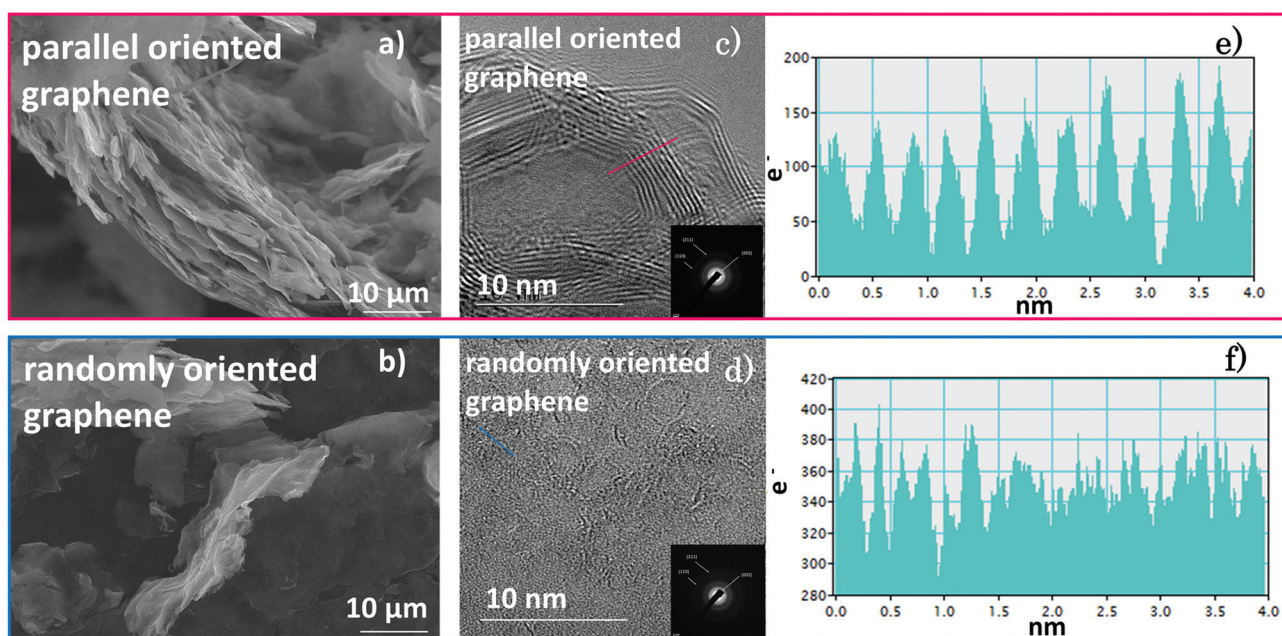

Fig. 2 Scanning electron microscopy (SEM) images of (a) parallel oriented graphene and (b) randomly oriented graphene. High-resolution transmission electron microscopy (HRTEM) images of (c) parallel oriented graphene and (d) randomly oriented graphene (insets are the electron diffraction patterns), (e) line profile of (c, f) line profile of (d).
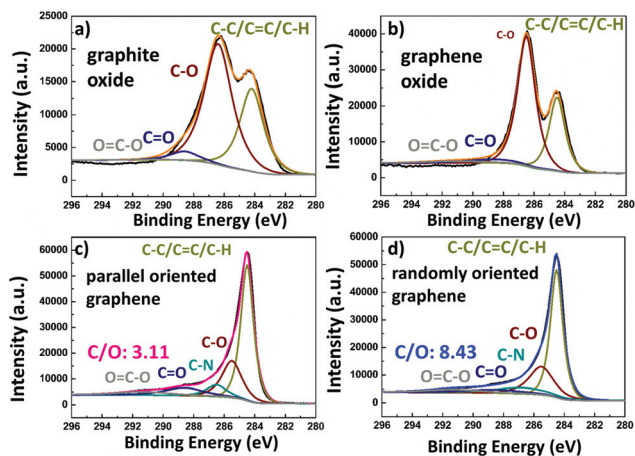
Fig. 3 X-ray photoelectron spectroscopy (XPS) C 1s spectra of (a) graphite oxide, (b) graphene oxide, (c) parallel oriented graphene and (d) randomly oriented graphene.
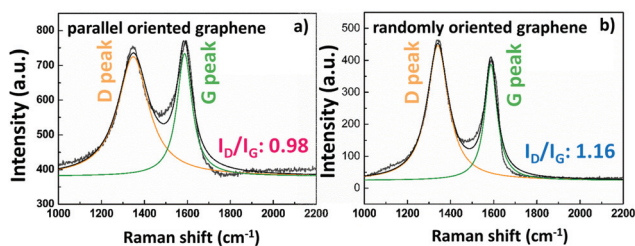

Fig. 4 Raman spectra of (a) parallel oriented graphene and (b) randomly oriented graphene.

C–C, C=C, and C–H bonds: 284.5 eV; C–N bonds: 285.5 eV; C–O bonds: 286.5 eV; C=O bonds: 288.6 eV and carboxyl groups O=C–O: 291.3 eV (ref. 24)). Carbon combined with O in POG and ROG has much lower peaks than in graphite oxide and graphene oxide, respectively, indicating the removal of oxygen-containing groups in graphite oxide and graphene oxide. This result can also be confirmed by the C and O contents listed in Fig. S2.† The C/O ratio of ROG is 8.43, which is much higher than that of POG (3.11). This result indicates a lower degree of reduction for POG than for ROG, similar to a previous result.[14]

Raman spectroscopy is an integral technique for analysing sp²-bonded carbon allotropes, especially for the discussion of defects and disorders.[25] As shown in Fig. 4, the Raman spectra of both materials show two typical peaks. The D peak corresponds to the breathing modes of carbon six-atom rings (requires defects for activation); the G peak is due to high-frequency E_{2g} phonons at the Brillouin zone centre Γ. The calculated I_D/I_G ratio (the height of the D peak (I_D) to the height of the G peak (I_G)) is an indicator to analyse the structure quality of carbon samples.[25] As shown in Fig. 4, the I_D/I_G ratio of POG is 0.98, much smaller than that of ROG (1.16). This phenomenon indicates an increased number of defect sites in ROG, which may be caused by the defect-rich graphene oxide.
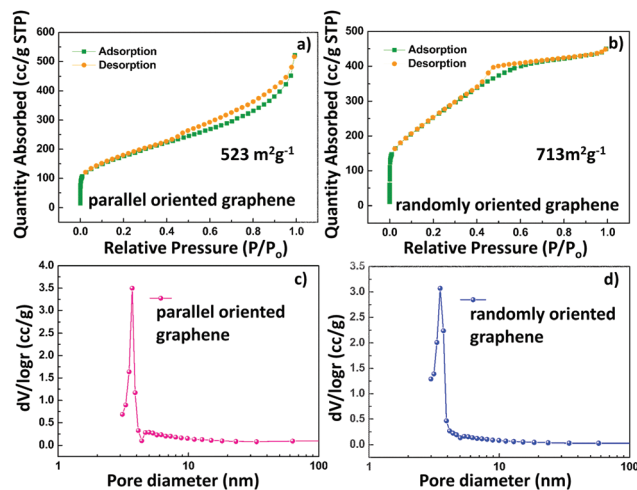

Fig. 5 Nitrogen sorption isotherms of (a) parallel oriented graphene and (b) randomly oriented graphene; corresponding pore size distributions of (c) parallel oriented graphene and (d) randomly oriented graphene.

All the features displayed in these characterizations agree with what is known for graphene samples, indicating that there are slight differences in the chemical compositions of the graphene produced from graphite oxide and graphene oxide.

Fig. 5(a) and (b) are the N_2 vapour pressure isotherms obtained for the two graphene samples. Both materials exhibit type IV isotherms with a hysteresis loop, indicating capillary condensation of gaseous molecules in the presence of mesopores in the materials. The pore sizes derived from the isotherms for both graphene samples are very similar; that of POG is 3.5 nm and that of ROG is 3.7 nm, as shown in Fig. 5(c) and (d). The plateau displayed in the isotherm in Fig. 5(a) indicates that the mesopores in POG have more uniform pore structures than those in ROG. However, the specific surface areas in POG and in ROG are quite different. The specific surface area of POG is 523 m² g⁻¹, while that of ROG is 713 m² g⁻¹, about 50% higher than that of POG (and much higher than that of graphite in Fig. S3†). Note that both these specific surface areas are much lower than the surface area estimated for single layer graphene (2600 m² g⁻¹); this probably means that both the POG and ROG samples consist of multilayer graphene sheets and those sheets restack together, preventing gaseous molecules from penetrating through the layers. The larger specific surface area of ROG in comparison to POG suggests that the graphene sheet structure in ROG is looser than that in POG.

3.3 Lithium intercalation

For LIB applications, it is important to compare the changes in the configuration and morphology of materials before and after lithium intercalation. To prevent reaction of the samples with air, an airtight sample chamber was used; Fig. 6(a) shows
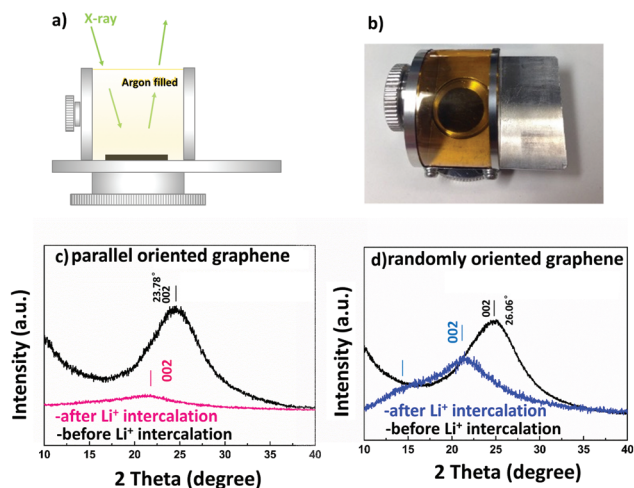
Fig. 6 (a) Schematic and (b) an image of the airtight sample chamber for X-ray diffraction (XRD) tests used in this study. Comparison of the X-ray diffraction patterns before and after lithium ion intercalation: (c) parallel oriented graphene and (d) randomly oriented graphene.

a sketch of the sample chamber. The chamber was filled with argon gas during the measurements.

The X-ray diffraction spectra of graphene, graphite oxide, graphene oxide, and graphite for comparison are shown in Fig. S4.† As shown in the black curves in Fig. 6(c) and (d), both POG and ROG exhibit typical broad peaks of amorphous patterns before lithium intercalation. The ROG shows the 002 peak at a higher position (26.06°) than POG (23.78°), indicating that ROG has a smaller d_{002} (0.342 nm, similar to ref. 26) than POG (0.374 nm). These results are in good agreement with the HRTEM image in Fig. 2. The smaller inter-layer spacing d_{002} of ROG can be explained by the high degree of reduction and the presence of fewer functional groups (Fig. 3) compared with POG. After lithium intercalation, all XRD absolute intensities of the (002) face for POG (Fig. 6(c)), ROG (Fig. 6(d)) and graphite (Fig. S5†) decreased. This result suggests lower degrees of periodicity on the (002) face, which results from the randomly arranged structures after lithium intercalation. Meanwhile, after lithium intercalation, the intensity of the (002) diffraction peak decreases and the peak position shifts towards a lower angle, suggesting that lithium intercalation causes expansion to the inter graphene sheets and introduces additional disorder to the morphology of the graphene sheet assembly. The d_{002} for graphite increases by about 10%, with increased lattice parameters (Fig. S6†). This result is similar to that in a previous study.[27] For the POG material, the d_{002} increased from 0.374 nm to 0.425 nm, as shown in Fig. 6(c) and S6(c)† (0.415 nm and 0.508 nm for ROG, as shown in Fig. 6(d) and S6(d)†).

In summary, structural and chemical differences exist between POG (reduction products from graphite oxide) and ROG (reduction products from graphene oxide). These differences arise from the dissimilarities between graphite oxide
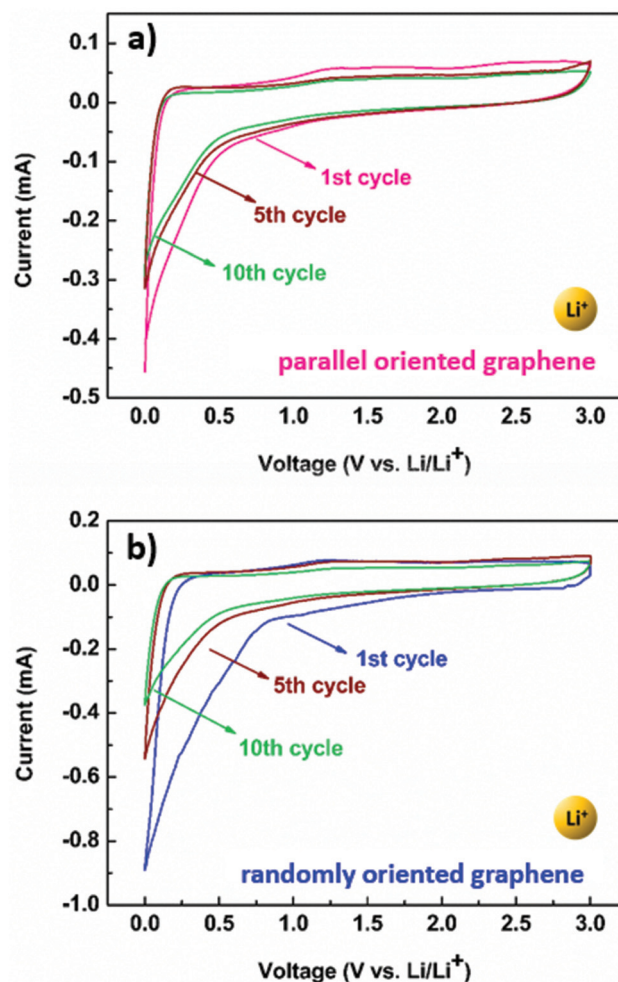

Fig. 7 Cyclic voltammogram curves of (a) parallel oriented graphene (POG) and (b) randomly oriented graphene at a potential scan rate of 0.1 mV s⁻¹ in lithium-ion batteries.

and graphene oxide. Therefore, these distinct characteristics will affect their applications, as discussed below.

3.4 Electrochemical performance in lithium-ion batteries

Fig. 7 depicts cyclic voltammogram (CV) curves measured on POG (a) and ROG (b) in a series of consecutive cycles measured at a scan rate of 0.1 mV s⁻¹. Both electrodes show broad reduction and oxidation peaks compared with graphite (Fig. S7(a)†). This result indicates typical features of nano-size carbonaceous materials as anodes in LIBs.[3] As shown in Fig. 7(a), the CV profile of POG after the initial cycle was steady from the 5th cycle to the 10th cycle. This indicates the high stability of POG, leading to high reversibility for lithium intercalation and de-intercalation. In contrast, ROG showed high instability during cycling, as shown in Fig. 7(b), as a result of the unstable structure of ROG. This unstable structure is due to weakened interlayer interactions after full exfoliation to form graphene oxide.

Fig. 8 shows the galvanostatic charge and discharge curves for POG (a) and ROG (b) measured in a series of cycles. Again,
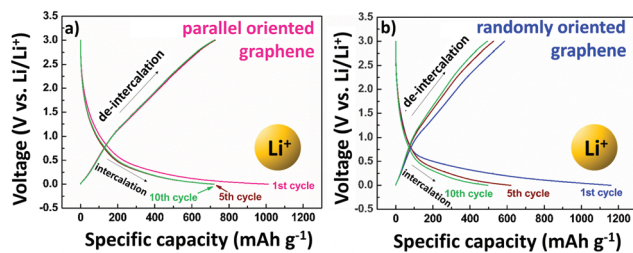
Fig. 8 Galvanostatic charge−discharge curves of (a) parallel oriented graphene and (b) randomly oriented graphene at 50 mA g^{-1} in lithium-ion batteries.

these figures show much smaller changes in the curve for POG after the first cycle than for ROG, indicating that POG is much more stable than ROG. Compared with the charge and discharge curves of graphite (Fig. S7(b)†), which have obvious plateaus, all the charge and discharge curves of POG and ROG show no distinguishable plateaus, indicating the presence of "electrochemically and geometrically nonequivalent Li ion sites".[26] For example, the lithium can: (i) be deposited as a multilayer,[28] (ii) be stored on both sides of a single layer,[29] (iii) react with defects and then drop to the edge[30] or surface.[31] The first discharge capacity of ROG was 1159 mA h g^{-1}, while the first charge capacity was only 586 mA h g^{-1} (49% irreversible capacity loss) due to the consumption of lithium ions during formation of the solid electrolyte interphase (SEI) film on the surface of the electrode.[3] As shown in Fig. 8(a), the first charge capacity of POG was 633 mA h g^{-1}, indicating 39% irreversible capacity loss. The lower irreversible capacity loss of POG was due to its smaller specific surface area, as shown in Fig. 5, because irreversible capacity loss is proportional to the surface area.[32] POG shows better stability than ROG during cycling, in agreement with Fig. 7.

The most striking difference in the performances of the electrodes fabricated with POG and ROG is demonstrated in Fig. 9, which shows the specific capacity (the charge that can be obtained under specified discharge conditions per gram) as a function of cycling history. The reversible capacity of ROG decreases dramatically from 586 to 316 mA h g^{-1} up to 100 cycles, which may be due to the instability of ROG. The charge capacity of POG decreased during the first several cycles, which is a normal characteristic, followed by a significant increase as the cycling continued. The charge capacity reached 917 mA h g^{-1} in the 77th cycle and then remained stable. This may be the result of a further increase in the d-spacing during cycling. The effects of lithium ion intercalation and de-intercalation may expand the interlayers. Then, these expanded interlayers can further increase the storage of lithium ions. Additionally, after 100 cycles, the resistance of the electrode decreases from 146 Ω to 102 Ω; this may be the result of further reduction during lithium ion intercalation and de-intercalation. This results in a low reduction degree of POG and increases the conductivity as well as the capacity during cycling. The coulombic efficiency of POG (Fig. 9(b)) is greater and more stable than that of ROG, indicating the structural
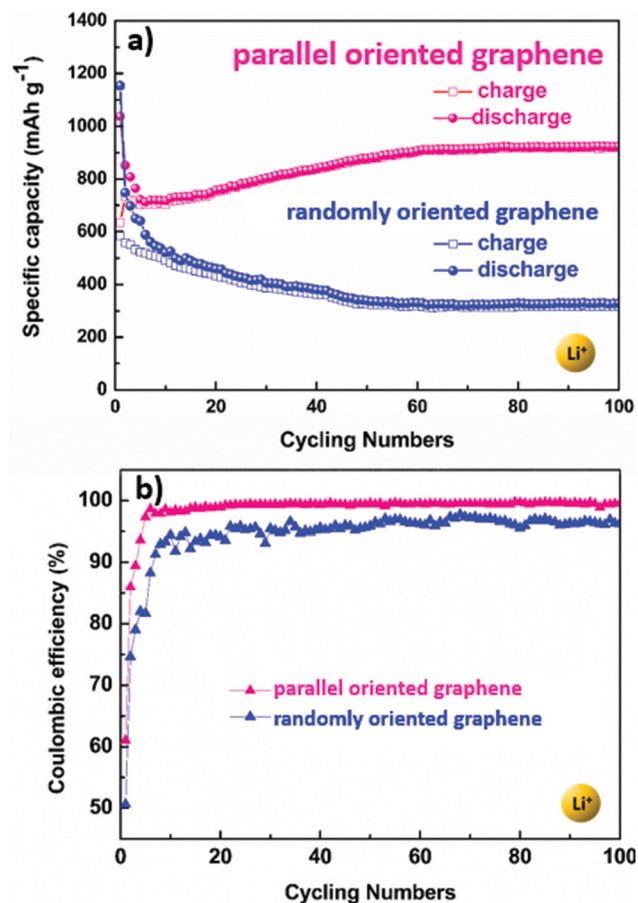

Fig. 9 (a) Cycling performance at a current density of 50 mA g^{-1} and (b) coulombic efficiency of parallel oriented graphene and randomly oriented graphene in lithium-ion batteries.

stability of POG compared with ROG. These characteristic behaviours were reproducible for different POG and ROG electrodes.

Furthermore, the POG electrode material exhibits better rate performance. As shown in Fig. 10, the POG electrode delivers charge capacities of 733, 582, 481, 385, and 327 mA h g^{-1} at current densities of 50, 100, 200, 500 and 1000 mA g^{-1}, respectively. These are much higher than the values for ROG and graphite (Fig. S7(e)†). Remarkably, compared with ROG, the stable capacity of POG can be resumed when the current density is reduced back to 50 mA g^{-1}. This may be due to the stable pathways for lithium intercalation and de-intercalation in POG. In contrast, the capacity of ROG cannot be recovered (only 276 mA h g^{-1}). This can be explained by the destroyed lithium intercalation channels of ROG, as shown in Fig. 6 and S6.†

3.5 Lithium ion diffusion coefficient and exchange current density calculations

To understand the kinetic properties of lithium transport in both electrodes, Fig. 11 compares the electrochemical impedance spectra of POG and ROG at the 50% state of charge
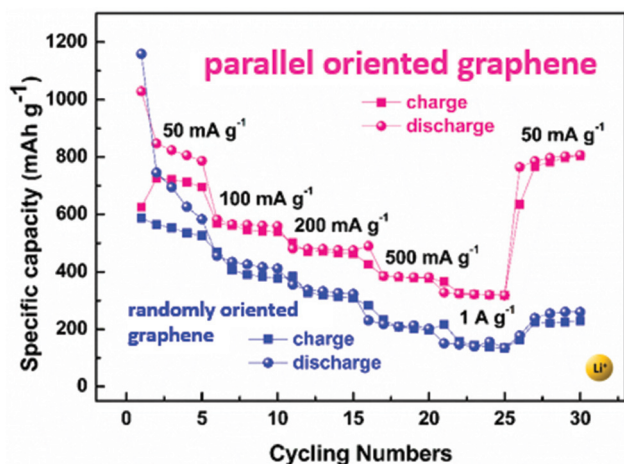
Fig. 10 Rate capabilities of parallel oriented graphene and randomly aggregated graphene as anodes in lithium-ion batteries.

Table 2 Studies on carbon anode materials in lithium-ion batteries

No.	Sample	d-Spacing (nm)	Charge capacity (mA h g^{-1})	Ref.
1	Graphite	0.335	320	26
2	Graphene	0.365	544	26
3	GNS + CNT	0.400	730	26
4	GNS + C60	0.400	784	26
5	Carbotron PS(F)	0.379	530	27
6	Carbotron P (F)	0.380	511	27
7	C nanofiber	0.336	598	36
8	Graphene layers	0.370	650	37
9	GNS	0.390	860	38
10	POG	0.374	917	This work

the diffusion process of lithium ions, corresponding to Z_w (Warburg impedance).[20] Table 1 shows that the R_{ct} of POG (67.92 Ω) is much smaller than that of ROG (312.08 Ω), indicating the greater lithium-ion conductivity of POG.

The calculated exchange current densities j_0 and lithium ion diffusion coefficients D_{Li} are summarized in Fig. 11(c), (d) and Table 1. The lithium ion diffusion coefficient of POG is 2.12×10^{-11} cm^2 s^{-1}; however, that of ROG is only 0.55×10^{-11} cm^2 s^{-1} (about 25% that of POG). This is because the lithium-ion diffusion in "the direction parallel to the graphene plane" (in-plane diffusion) is much greater than the cross-plane lithium-ion diffusion.[34,35] As shown in Fig. 1(b), the in-plane diffusion for ROG is limited (short green solid lines). Because the cross-plane diffusion (short blue dotted line) contributes only slightly to the total lithium-ion diffusion, the lithium-ion diffusion of ROG is low. In contrast, POG, which has a parallel oriented structure, can support efficacious channels for lithium diffusion, as shown in Fig. 1(b). The exchange current density j_0 of POG is 9.28×10^{-4} A cm^{-2}, which is about 5 times greater than that of ROG. This result is coherent with those shown in Fig. 7 and 8, indicating the high reversibility of the electrochemical reaction for POG due to its high structural stability. Thus, POG exhibits more favorable kinetic properties compared with ROG. Compared with other carbon anodes in LIBs, POG exhibits comparable performance, as shown in Table 2; this indicates that POG is a promising candidate with great potential for use in lithium-ion batteries.

3.6 Electrochemical performance in sodium-ion batteries

Because the storage mechanism of sodium ions in carbon materials is similar to that of lithium ions,[39] it is logical to apply graphene electrodes as anodes for sodium-ion batteries. Na$^+$ is about 55% larger than Li$^+$. The high accommodation of lithium ions in graphite is not feasible for sodium ions. Therefore, most anodes in LIBs, such as graphite, are not appropriate for sodium-ion batteries (SIBs).[40] For SIBs, a key factor in the anode is to have sufficiently large interlayer spacing to host sodium ions. Theoretical calculations have demonstrated that a minimum interlayer distance of 0.37 m is requited for sodium ion intercalation and de-intercalation.[40,41] A higher specific capacity can be achieved though graphene with nitrogen doping[42] and phosphorus/graphene[43] hybrid
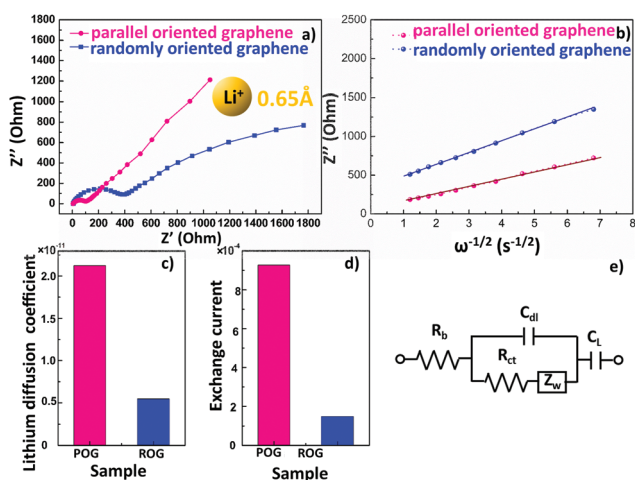

Fig. 11 Electrochemical impedance spectroscopy in lithium-ion batteries: (a) Nyquist plots, (b) the relationship between Z' and $\omega^{-1/2}$ at the low frequency region, (c) lithium diffusion coefficients (D_{Li}), (d) exchange currents (j_0) of parallel oriented graphene and randomly oriented graphene at the 50% state of charge (SOC) of the 10th cycle; (e) equivalent circuit used to model the obtained impedance spectra. R_b is the equivalent circuit resistance, R_{ct} is the charge-transfer resistance, C_{dl} is the constant phase element, which refers to the electric double-layer capacitance in nonhomogeneous systems, Z_w is the Warburg impedance, which relates to the diffusion of lithium ions in the solid, and C_L is the intercalation capacitance.

(SOC) of the 10th cycle. As shown in Fig. 11(a), both electrodes show a semicircle in the high frequency region and a line in the low frequency region. In order to perform quantitative analysis, an equivalent circuit for this mode[21,33,34] was used (Fig. 11(d)). The high-frequency semicircle reflects the migration process of lithium ions, corresponding to R_{ct} (charge-transfer resistance) and C_{dl} (constant phase element, which refers to the electric double-layer capacitance in nonhomogeneous systems). The low frequency sloping line reflects
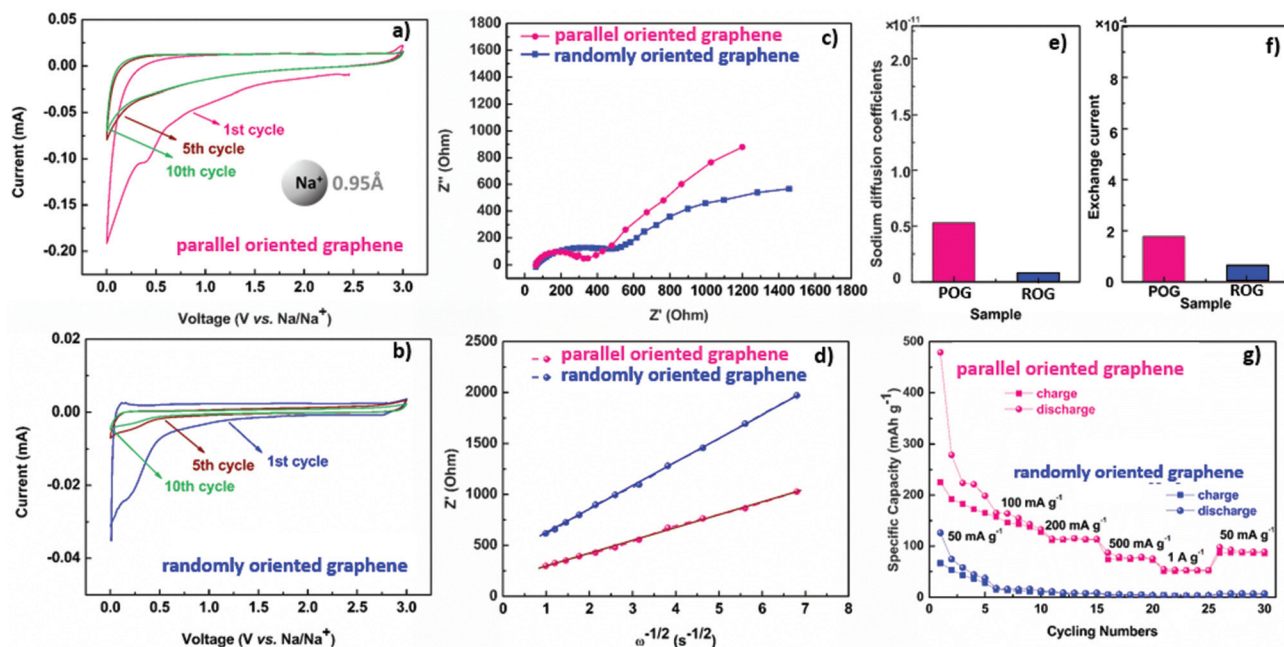
Fig. 12 Electrochemical performance in sodium-ion batteries: cyclic voltammogram curves of (a) parallel oriented graphene (POG) and (b) randomly oriented graphene at a potential scan rate of 0.1 mV s^{-1}, (c) Nyquist plots, (d) the relationship between Z' and $\omega^{-1/2}$ in the low frequency region, (e) sodium diffusion coefficients (D_{Na}), (f) exchange currents (j_0) of parallel oriented graphene and randomly oriented graphene at the 50% state of charge (SOC) of the 10th cycle, (g) rate capabilities of parallel oriented graphene and randomly oriented graphene as anodes in sodium-ion batteries.

structures. In this work, the differences in the sodium ion intercalation/de-intercalation behaviour between POG and ROG are very obvious, as shown in Fig. 12.

Fig. 12(a) and (b) compare the first, fifth and tenth CV curves of POG and ROG at a scan rate of 0.1 mV s^{-1} between 0.01 and 3 V (*vs.* Na/Na$^+$). In the first cycle, similar to carbon nanowires in ref. 40, both electrode materials show a small irreversible peak at about 0.4 V *versus* Na/Na$^+$, related to the SEI film formation. The CV curves of ROG tend to decrease dramatically after the first cycle. Meanwhile, the CV curves of the POG anode decay slightly between the fifth and tenth cycles, indicating the stability of POG during sodium ion intercalation and de-intercalation. Similar to the Nyquist plots of lithium ion diffusion shown in Fig. 11(a) and (b), both electrodes exhibit one semicircle and one line in the high and low frequency regions in SIBs, respectively. As shown in Fig. 12(c) and Table 1, the R_{ct} values for both anodes during sodium ion intercalation and de-intercalation are dramatically increased, indicating smaller sodium conductivity compared with lithium conductivity. Fig. 12(e) and (f) show the calculated sodium ion diffusion coefficients D_{Na} and the exchange current densities j_0. Compared with the lithium ion diffusion coefficients D_{Li}, the sodium ion diffusion coefficients D_{Na} for both electrodes are smaller due to the larger radius of sodium ions. Because the insertion processes for both lithium ions and sodium ions are accompanied by an increase in the interlayer spacing in carbon materials,[40] the D_{Na} of POG is much greater than that of ROG (about 5.4 times greater). The

exchange current densities j_0 of both anodes in SIBs are smaller than those in LIBs. This decrease of exchange current density indicates lower reversibility of the electrochemical reaction in SIBs compared with that in LIBs. Although the specific capacity of both anodes in SIBs (Fig. 12(g)) is low, the rate performance of POG is much better than that of ROG in SIBs. As shown in Fig. 12(g), the reversible capacities of POG at various rates were 225, 157, 112, 73 and 51 mA h g^{-1} at increasing current densities of 50, 100, 200, 500 mA g^{-1} and 1 A g^{-1}, respectively, comparable with the carbon spheres reported in ref. 44. In contrast, the charge capacities of ROG were very limited. The charge capacity of ROG is 27 mA h g^{-1} at a current density of 50 mA g^{-1}, similar to that of graphite, as reported in ref. 39 and 40.

In summary, from the above comparisons, it can be concluded that there are differences between the reduction products of graphite oxide and graphene oxide. These structural and chemical differences result in different electrochemical behaviours in lithium-ion batteries and sodium-ion batteries.

4.   Conclusions

In summary, we have synthesized graphene *via* direct reduction of graphite oxide and *via* reduction of graphene oxide. We found that the graphene produced *via* direct reduction of graphite oxide maintained a certain degree of layer morphology. X-ray deflection measurements showed that

the d-spacing (d_{002}) in reduced graphite oxide is greater than that in reduced graphene oxide, giving rise to wide transportation channels for ions. Lithium ion batteries with reduced graphite oxide as the anode reached a specific capacity of 917 mA h g^{-1}, which is almost twice that of reduced graphene oxide. The reduced graphite oxide showed a smaller surface area and fewer defects compared with reduced graphene oxide. In addition to the structural and chemical differences between reduced graphite oxide and reduced graphene oxide, the kinetic properties of both electrodes for lithium ion diffusion and sodium ion diffusion were analysed. The results show that reduced graphite oxide exhibits much greater lithium-ion and sodium-ion coefficients compared with reduced graphene oxide. The electrochemical performances of lithium-ion batteries and sodium-ion batteries with reduced graphite oxide anodes show noticeable improvements compared to those with reduced graphene oxide anodes. We find that reduced graphite oxide may be a more favourable form of graphene for the fabrication of electrodes for lithium/sodium ion batteries and other energy storage devices.

Acknowledgements

References

1 M. Wakihara and O. Yamamoto-Weinheim, *Lithium Ion Batteries: Fundamentals and Performance*, Wiley-VCH, Berlin, New York, Chichester, Brisbane, Singaporo, Toronto, 1998.

2 X.-X. Yuan, H.-S. Liu and J.-J. Zhang, *Lithium-ion Batteries: Advanced Materials and Technologies*, CRC Press, Boca Raton, London, New York, 2011.

3 Z. S. Wu, W. Ren, L. Xu, F. Li and H.-M. Cheng, *ACS Nano*, 2011, **7**, 5463–5471.

4 Q.-G. Shao, W.-M. Chen, Z.-H. Wang, L. Qie, L.-X. Yuan, W.-X. Zhang, X.-L. Hu and Y.-H. Huang, *Electrochem. Soc.*, 2011, **13**, 1431–1434.

5 T. Zheng, Y. Liu, E. W. Fuller, S. Tseng, U. von Sacken and J. R. Dahn, *J. Electrochem. Soc.*, 1995, **142**, 2581–2590.

6 J. R. Dahn, R. Fong and M. J. Spoon, *Phys. Rev. B: Condens. Matter*, 1990, **42**, 6424–6432.

7 H. Shi, J. Barker, M. Y. Saïdi, R. Koksbang and L. Morries, *J. Power Sources*, 1997, **68**, 291–295.

8 X. Wang, X. Zhou, K. Yao, J. Zhang and Z. Liu, *Carbon*, 2011, **49**, 133–139.

9 A. K. Geim and K. S. Novoselov, *Nat. Mater.*, 2007, **6**, 183–191.

10 L. Ye, Q. Liang, Y. Lei, X. Yu, C. Han, W. Shen, Z.-H. Huang, F. Kang and Q.-H. Yang, *J. Power Sources*, 2015, **282**, 174–178.

11 S. Stankovich, D. A. Dikin, R. D. Piner, K. A. Kohlhaas, A. Kleinhammes, Y. Jia, Y. Wu, S. T. Nguyen and R. S. Ruoff, *Carbon*, 2007, **45**, 1558–1565.

12 F. Zhang, J. Tang, N. Shinya and L.-Ch. Qin, *Chem. Phys. Lett.*, 2013, **584**, 124–129.

13 D. R. Dreyer, S. Park, C. W. Bielawski and R. S. Ruoff, *Chem. Soc. Rev.*, 2010, **39**, 228–240.

14 S. Park, J. An, J. R. Rotts, A. Velamakanni, S. Murali and R. S. Ruoff, *Carbon*, 2011, **49**, 3019–3023.

15 P. Ge and M. Fouletier, *Solid State Ionics*, 1988, **28-30**, 1172–1175.

16 T. Szabó, O. Berkesi, P. Forgó, K. Josepovits, Y. Sanakis, D. Petridis and I. Dékány, *Chem. Mater.*, 2006, **18**, 2740–2749.

17 A. Lerf, H. He, M. Forster and J. Klinowski, *J. Phys. Chem. B*, 1998, **102**, 4477–4482.

18 W. Gao, L. B. Alemany, L. Ci and P. M. Ajayan, *Nat. Chem.*, 2009, **1**, 403–408.

19 J. Chen, B. Yao, C. Li and G. Shi, *Carbon*, 2013, **64**, 225–229.

20 S. Yang, J. Huo, H. Song and X. Cheng, *Electrochim. Acta*, 2008, **53**, 2238–2244.

21 K. Dokko, M. Mohamedi, Y. Fujita, T. Itoh, M. Nishizawa, M. Umeda and I. Uchida, *J. Electrochem. Soc.*, 2001, **148**, A422–A426.

22 X. Wang, H. Hao, J. Liu, T. Huang and A. Yu, *Electrochim. Acta*, 2011, **56**, 4065–4069.

23 L. Wang, J. Zhao, X. He, J. Gao, J. Li, C. Wang and C. Jiang, *Int. J. Electrochem. Sci.*, 2012, **7**, 345–353.

24 H. Yan, C. Tian, L. Sun, B. Wang, L. Wang, J. Ying, A. Wu and H. Fu, *Energy Environ. Sci.*, 2014, **7**, 1939–1949.

25 A. C. Ferrari and D. M. Basko, *Nat. Nanotechnol.*, 2013, **8**, 235–246.

26 E. Yoo, J. Kim, E. Hosono, H.-S. Zhou, T. Kudo and I. Honma, *Nano Lett.*, 2008, **8**, 2277–2282.

27 H. Shioyama, *Synth. Met.*, 2000, **114**, 1–15.

28 R. Yazami and M. Deschamps, *J. Power Sources*, 1995, **54**, 411–415.

29 J. S. Xue and J. R. Dahn, *J. Electrochem. Soc.*, 1995, **142**, 3668–3677.

30 S. Wang, Y. Matsumura and T. Maeda, *Synth. Met.*, 1995, **71**, 1759–1760.

31 B. Huang, Y. Huang, Z. Wang, L. Chen, R. Xue and F. Wang, *J. Power Sources*, 1996, **58**, 231–234.

32 P. Novák, F. Jonoo, M. Lanz, B. Rykart, J.-C. Panitz, D. Alliata, R. Kotz and O. Haas, *J. Power Sources*, 2001, **97-98**, 39–46.

33 Y. Sun, C. Xu, B. Li, J. Zao, Y. He, H. Du and F. Kang, *Int. J. Electrochem. Sci.*, 2014, **9**, 6387–6401.

34 X. Zhao, C. M. Hayner, M. C. Kung and H. H. Kung, *ACS Nano*, 2011, **5**, 8739–8749.

35 K. Persson, V. A. Sethuraman, L. J. Hardwick, Y. Hinuma, Y. S. Meng, A. V. D. Ven, V. Srinivasan, R. Kostecki and G. Ceder, *J. Phys. Chem. Lett.*, 2010, **1**, 1176–1180.

36 K. Gotoh, M. Maeda, A. Nagai, A. Goto, M. Tansho, K. Hashi, T. Shimizu and H. Ishida, *J. Power Sources*, 2006, **162**, 1322–1328.

37 S.-H. Yoon, C.-W. Park, H. Yang, Y. Korai, I. Mochida, R. T. K. Baker and N. M. Rodriguez, *Carbon*, 2004, **42**, 21–32.

38 G. Wang, X. Shen, J. Yao and J. Park, *Carbon*, 2009, **47**, 2049–2053.

39 D. A. Stevens and J. R. Dahn, *J. Electrochem. Soc.*, 2001, **148**, A803–A811.

40 Y. Cao, L. Xiao, M. L. Sushko, W. Wang, B. Schwenzer, J. Xiao, Z. Nie, L. V. Saraf, Z. Yang and J. Liu, *Nano Lett.*, 2012, **12**, 3783–3787.

41 Y.-X. Wang, S.-L. Chou, H.-K. Liu and S.-X. Dou, *Carbon*, 2013, **57**, 202–208.

42 H.-G. Wang, Z. Wu, F.-L. Meng, D.-L. Ma, X.-L. Huang, L.-M. Wang and X.-B. Zhang, *ChemSusChem*, 2013, **6**, 56–60.

43 J. Song, Z. Yu, M. L. Gordin, S. Hu, R. Yi, D. Tang, T. Walter, M. Regul, D. Choi, X. Li, A. Manivannan and D. Wang, *Nano Lett.*, 2014, **14**, 6329–6335.

44 K. Tang, L. Fu, R. J. White, L. Yu, M.-M. Titirici, M. Antonietti and J. Maier, *Adv. Energy Mater.*, 2012, **2**, 873–877.